remote sensing

MDPI

Article

Multispectral Optical Diagnostics of Lightning from Space

Francisco J. Pérez-Invernón [1,*], Francisco J. Gordillo-Vázquez [1], María Passas-Varo [1], Torsten Neubert [2], Olivier Chanrion [2], Victor Reglero [3] and Nikolai Østgaard [4]

[1] Instituto de Astrofísica de Andalucía (IAA-CSIC), Glorieta de la Astronomía s/n, 18008 Granada, Spain; vazquez@iaa.es (F.J.G.-V.); passasv@iaa.es (M.P.-V.)
[2] National Space Institute, Technical University of Denmark (DTU Space), 2800 Kongens Lyngby, Denmark; neubert@space.dtu.dk (T.N.); chanrion@space.dtu.dk (O.C.)
[3] Image Processing Laboratory, University of Valencia, 46010 Valencia, Spain; victor.reglero@uv.es
[4] Birkeland Centre for Space Science, Department of Physics and Technology, University of Bergen, 5007 Bergen, Norway; nikolai.ostgaard@uib.no
* Correspondence: fjpi@iaa.es

Abstract: We present spectroscopic diagnostic methods that allow us to estimate the gas and the electron temperature in emerged lightning stroke channels (from thunderclouds) observed by the photometers and cameras of the Atmosphere Space Interaction Monitor (ASIM). We identify the species (molecules, atoms and ions) producing light emission in different wavelengths, and how the blue (337 $\pm$ 2 nm), red (777.4 $\pm$ 2.5 nm) and ultraviolet (180–230 nm) optical emissions captured by ASIM photometers change as a function of the temperature in the lightning stroke channel. We find good agreement between the light curves of the emerged lightning observed by ASIM and the synthetic ones obtained from calculated spectra. Our results suggest that (i) early stage (high temperature $>$ 20,000 K) emerged lightning strokes at high altitude can contribute to the optical signals measured by the PH2 photometer (180–230 nm), (ii) intermediate stage (mid temperatures, 6000–21,000 K) emerged lightning strokes can produce 777.4 nm near-infrared radiation (observable by PH3) exhibiting higher intensity than PH1 observable N_2 SPS between ∼6000 K and ∼8000 K, and than ion optical emissions (336.734 nm and 337.714 nm) between ∼16,000 K and ∼21,000 K, (iii) from ∼16,000 K to 35,000 K, neutral oxygen 777.4 nm radiation and ion emissions at 336.734 nm and 337.714 nm can be simultaneoulsy observed but 777.4 nm dominates only between ∼16,000 K and ∼21,000 K, (iv) the availability of detections with a narrow 0.5 nm gap filtered photometer (336.75–337.25 nm), with the same or better sensitivity than PH1 in ASIM-MMIA but with a central wavelength at exactly 337.0 nm (the strongest N_2 SPS transition), would give access to the late stage of lightning strokes (emerged or not) when temperatures are between 8000 K and 5000 K (or lower for a photometer with better sensitivity than PH1 in ASIM-MMIA) when the production of nitrogen oxides (NO_x) and hydroxyl radicals (OH) maximizes.

Keywords: lightning spectra from space; multispectral optical diagnostics; thermal non-equilibrium; ASIM; lightning channel gas temperature; lightning ultraviolet optical emissions

Citation: Pérez-Invernón, F.J.; Gordillo-Vázquez, F.J.; Passas-Varo, M.; Neubert, T.; Chanrion, O.; Reglero, V.; Østgaard, N. Multispectral Optical Diagnostics of Lightning from Space. *Remote Sens.* **2022**, *14*, 2057. https://doi.org/10.3390/rs14092057

Academic Editors: Stefano Federico, Gaopeng Lu, Yang Zhang and Fanchao Lyu

Received: 8 April 2022
Accepted: 23 April 2022
Published: 25 April 2022

1. Introduction

Remote sensing instruments have significantly provided new insights into the physics of atmospheric electricity phenomena in the last few decades. The Optical Transient Detector (OTD) was a starting imager devoted to lightning detection from the MicroLab-1 satellite operating between 1995 and 2000 [1]. Similarly, the Lightning Imaging Sensor (LIS) is a charge-coupled device (CCD) array operated on the Tropical Rainfall Measuring Mission (TRMM) satellite between 1997 and 2017 [2] and from the International Space Station (ISS) since March 2017 [3]. The filters of OTD and LIS are centered on the neutral atomic oxygen multiplet at 777.4 nm, a prominent line in lightning spectra [4]. Measurements provided by OTD/LIS have represented a considerable advance in remote sensing

techniques of lightning. In particular, the 2 ms integration time observations of OTD and LIS have contributed to provide unprecedented global climatologies of lightning and its characteristics, such as the total number of pulses per flash, the radiance per flash and the flash duration [5]. Geostationary satellites are starting to contribute with new valuable information about these lightning variables (e.g., [6–8]). However, OTD/LIS and typical geostationary satellites are equipped with a single wavelength (777.4 nm) sensor able to monitor the occurrence of total lightning but not suitable to perform multispectral measurements that could contribute to advance the knowledge and diagnostics of the different temporal stages of the heated channel of lightning strokes.

Chang et al. (2010) [9] calculated the synthetic spectra of lightning to analyze the optical signal detected by the 10 kHz sampling rate photometers onboard the Imager of Sprites and Upper Atmospheric Lightnings (ISUAL). The synthetic spectra allowed them to estimate the contribution of the heated lightning channels to the photometers. They concluded that the optical signal emitted by lightning was not detectable by the Far UltraViolet (FUV) photometer of ISUAL looking at the limb due to atmospheric absorption. Adachi et al. (2009) [10] employed ISUAL measurements to estimate the temporal evolution of the electric current of lightning from space.

The optical signals emitted by lightning can be produced by streamer-coronas, leaders and/or return strokes [11]. The gas temperature of streamer-coronas is similar to the ambient temperature but the electron mean energy (temperature) is much higher. Thus, the main optical emissions of streamers are mainly produced by electron impact collisions with chemical species in the air and the subsequent decay of electronic–vibrational–rotational excited states of the molecular species in air (N_2, O_2) or of their dissociation products (OH, NO, NO_2, ...). On the contrary, leaders and return strokes are close to thermal-equilibrium plasmas with gas temperatures ranging between a few thousands of Kelvin and about 40,000 K. The high degree of thermal dissociation and ionization of the air in leaders and return strokes contribute to significant optical emissions from excited atoms (predominantly O, N and H) and ions [4,12–14], although molecular emissions are also measured [15]. Laboratory [12–14,16,17] and aircraft measurements [18,19] of the spectra of lightning and lightning-like discharges have proven to be very useful to extract interesting parameters of lightning discharges. The most commonly employed diagnostic methods of plasma discharges are based on spectroscopic quantities that do not depend on the absolute flux of photons. The advantage of this approach is that spectra measured in arbitrary units can be used. For example, the electron density of a thermal plasma can be estimated from the broadening of measured spectral lines [20,21], while the electron temperature can be calculated from the intensity ratio of a pair of measured spectral lines [13,22,23]. In addition, the electric field in non-equilibrium plasma discharges can also be estimated from the ratio of several spectral lines [24–29].

The Atmosphere Space Interactions Monitor (ASIM) [30] was mounted on the International Space Station (ISS) on 13 April 2018. The Modular Multispectral Imaging Array (MMIA) [31] onboard the nadir-looking (until January 2022) ASIM is devoted to investigating the optical signal of atmospheric electricity phenomena. The unprecedented high-sampling frequency (100 kHz) of the ASIM-MMIA photometers and the high spatial resolution cameras (400×400 m^2/pixel) provide a new opportunity to diagnose from space the light emissions produced by lightning-produced plasmas. Since April 2018, the MMIA instrument has provided optical measurements of lightning [32–34], blue discharges [35–38] and upper-mesospheric Transient Luminous Events (TLEs), such as elves, sprites or halos, Ref. [39] from a low Earth orbit. The optical signal emitted by lightning is frequently influenced by cloud scattering before reaching MMIA, as investigated by Luque et al. (2020) [40]. In this work, we analyze three events with an exposed lightning channel detected by the MMIA Photometers (PH) and Camera Head Units (CHU).

We present spectroscopic diagnostic methods that allow us to estimate the gas and the electron temperatures in exposed lightning channels from space-based photometers and camera measurements. We identify the species (molecules, atoms and ions) producing

light emission in different wavelengths and the predominance of blue (337 ± 2 nm), red (777.4 ± 2.5 nm) and ultraviolet optical emissions (180–230 nm) as a function of the temperature in the lightning channel. Finally, we calculate the source-radiated power (MW/m) in the visible (380–780 nm) and ultraviolet (100–380 nm) spectral ranges for different lightning channel temperatures.

2. Materials and Methods

2.1. Modular Multispectral Imaging Array Measurements

The MMIA instrument [31] onboard ASIM incorporates three photometers sampling at 100 kHz in the near UV line at 337 nm ± 2 nm (PH1), in the Ultra Violet (UV) band at 180–230 nm (PH2) and in the neutral atomic oxygen multiplet at 777.4 nm ± 2.5 nm (PH3). The MMIA instrument in ASIM is also equipped with two filtered cameras operating at 12 fps in the near UV (CHU1, 337 nm ± 2 nm) and in the neutral atomic oxygen multiplet (CHU2, 777.4 nm ± 2.5 nm) with a spatial resolution of 400 × 400 m^2/pixel. We show in Table 1 all the molecular, atomic and ionic transitions that can contribute to the photometers of ASIM-MMIA.

The ASIM-MMIA cameras allow us to determine the existence of exposed lightning channels in thunderstorms. We have selected three events with an exposed lightning channel where the ASIM-MMIA cameras show that the emitted optical signal did not travel through a significant cloud layer. The events were recorded on the 12 November 2018, the 12 December 2018 and the 2 April 2019 near Peru, Angola and the Philippines, respectively.

2.2. Cloud Top Height Products

We use the Cloud Top Height (CTH) products derived from satellite measurements to estimate the altitude of the analyzed exposed lightning channels. Depending on the location of each particular event, we use the CTH product derived from the Meteosat Second Generation (MSG) satellites over Europe and Africa [41], the Geostationary Operational Environmental Satellite R-Series 16 (GOES-16) CTH product over America or the Himawari-8 CTH product over Asia and the East of the Pacific Ocean. These geostationary satellites provide high spatially-resolved CTH products on the scale of a few of kilometers with a frequency of 15 min. We refer to Schmetz et al. (2002) [41], Liu et al. (2019) [42] and Huang et al. (2019) [43] for more details on the CTH products.

2.3. Spectroscopic Diagnostic Method

We have developed a diagnostic method to estimate the gas and the electron temperatures of exposed lightning channels from space-based measurements. The method is based on the calculation of synthetic spectra of lightning-like discharges given a pair of gas and electron temperatures. The calculation of the spectra initially relies on equilibrium calculations of thermal air plasmas. In this section, we present the calculation procedure for the emitted and the observed synthetic spectra (Section 2.3.1) and we explain how the ASIM-MMIA measurements can be used to estimate the gas and the electron temperature (Section 2.3.2) of the reported exposed lightning channel.

2.3.1. Calculation of Synthetic Spectra

The method to calculate synthetic spectra is based on equilibrium calculations of thermal air plasmas (see supplementary material of Kieu et al. (2020) [14] and Kieu et al. (2021) [15]). We perform Local Thermal Equilibrium (LTE) calculations in the temperature range 1000–35,000 K with a method based upon the mass action law and the chemical base concept [44,45] to estimate the equilibrium concentration and the internal partition functions of air species at 1 atm, 0.48 atm (nearly 5 km altitude), 0.27 atm (nearly 10 km altitude) and 0.012 atm (nearly 15 km altitude). The chemical species considered in the calculation are 14 atomic, 24 diatomic and 44 polyatomic species including electrons, negative ions, single and doubly ionized positive ions.

Table 1. Molecular, atomic and ionic transitions that can contribute to the ASIM-MMIA photometers.

Photometer	Molecular Transitions [46]	Atomic/Ionic Transitions [47]
PH1 (337/4 nm)	$N_2(C^3\Pi_u, v = 0) \rightarrow N_2(B^3\Pi_g, v = 0)$	O II (337.7146 nm) N II (336.734 nm)
PH2 (180–230 nm)	$N_2(a^1\Pi_g, v = 0) \rightarrow N_2(X^1\Pi_g^+, v = 6 \ldots 11)$, $N_2(a^1\Pi_g, v = 1) \rightarrow N_2(X^1\Pi_g^+, v = 7 \ldots 12)$, $N_2(a^1\Pi_g, v = 2) \rightarrow N_2(X^1\Pi_g^+, v = 8 \ldots 13)$, $N_2(a^1\Pi_g, v = 3) \rightarrow N_2(X^1\Pi_g^+, v = 9 \ldots 14)$, $N_2(a^1\Pi_g, v = 4) \rightarrow N_2(X^1\Pi_g^+, v = 9 \ldots 15)$, $N_2(a^1\Pi_g, v = 5) \rightarrow N_2(X^1\Pi_g^+, v = 10 \ldots 15)$, $N_2(a^1\Pi_g, v = 6) \rightarrow N_2(X^1\Pi_g^+, v = 11 \ldots 16)$, $N_2(a^1\Pi_g, v = 7) \rightarrow N_2(X^1\Pi_g^+, v = 12 \ldots 17)$, $N_2(a^1\Pi_g, v = 8) \rightarrow N_2(X^1\Pi_g^+, v = 12 \ldots 18)$, $N_2(a^1\Pi_g, v = 9) \rightarrow N_2(X^1\Pi_g^+, v = 13 \ldots 19)$, $N_2(a^1\Pi_g, v = 10) \rightarrow N_2(X^1\Pi_g^+, v = 14 \ldots 20)$, $N_2(a^1\Pi_g, v = 11) \rightarrow N_2(X^1\Pi_g^+, v = 15 \ldots 20)$, $N_2(a^1\Pi_g, v = 12) \rightarrow N_2(X^1\Pi_g^+, v = 15 \ldots 21)$, $N_2(a^1\Pi_g, v = 13) \rightarrow N_2(X^1\Pi_g^+, v = 16 \ldots 21)$, $N_2(a^1\Pi_g, v = 14 \rightarrow N_2(X^1\Pi_g^+, v = 17 \ldots 21)$, $N_2(a^1\Pi_g, v = 15) \rightarrow N_2(X^1\Pi_g^+, v = 17 \ldots 21)$	O II (182.1545 nm), O II (182.7276 nm), O II (182.9362 nm), O II (183.5906 nm), O II (189.3789 nm), O III (192.004 nm), O II (195.7441 nm), O II (195.8122 nm), O II (196.0265 nm), O II (196.2210 nm), O II (196.3793 nm), O II (196.4269 nm), O II (201.6589 nm), O II (202.0340 nm), O II (202.1445 nm), O II (202.3332 nm), O II (202.5694 nm), O II (202.7103 nm), O II (202.7603 nm), O II (207.22 nm), O II (207.2601 nm), O II (207.5169 nm), O II (209.2876 nm), O II (210.1283 nm), O II (212.3202 nm), O II (213.1818 nm), O II (213.1997 nm), O II (218.2580 nm), O II (219.0481 nm), O II (219.5464 nm), O II (221.5701 nm), O II (221.8679 nm), O II (224.9719 nm), O II (225.2746 nm), O II (225.9625 nm), O II (226.2685 nm), O II (228.3447 nm), O II (228.4836 nm), O II (229.0839 nm), O II (229.3301 nm), N III (180.4486 nm), N III (180.5669 nm), N III (184.642 nm), N III (188.506 nm), N III (188.522 nm), N III (190.799 nm), N III (191.955 nm), N III (191.977 nm), N III (192.065 nm), N III (192.084 nm), N III (192.130 nm), N III (206.401 nm), N III (208.034 nm), N II (209.553 nm), N II (209.620 nm), N II (209.686 nm), N III (211.759 nm), N III (211.150 nm), N II (213.018 nm), N II (214.278 nm), N III (214.731 nm), N II (220.609 nm), N II (228.669 nm), N II (228.844 nm)
PH3 (777.4/5 nm)	–	O I (777.194 nm). O I (777.417 nm). O I (777.539 nm), N II (776.224 nm)

The population of the electronic–vibrational–rotational excited states of molecular nitrogen $N_2(B^3\Pi_g, v = 0 \ldots 6, J = 0 \ldots J^B_{max})$, $N_2(C^3\Pi_u, v = 0 \ldots 4, J = 0 \ldots J^C_{max})$ and $N_2(a^1\Pi_g, v = 0 \ldots 15, J = 0 \ldots J^a_{max})$ are estimated from the calculated equilibrium concentrations and internal partition functions of N_2. The calculation of the $N_2(B^3\Pi_g, v = 0 \ldots 6, J = 0 \ldots J^B_{max})$, $N_2(C^3\Pi_u, v = 0 \ldots 4, J = 0 \ldots J^C_{max})$ and $N_2(a^1\Pi_g, v = 0 \ldots 15, J = 0 \ldots J^a_{max})$ concentrations are used to estimate the first positive system (FPS) in the visible—Near-infrared (500–1500 nm), the second positive system (SPS) in the near-UV-blue (250–450 nm) and the Lyman Birge Hopfield (LBH) system in the vacuum UV (120–230 nm), respectively.

We calculate the total energy of molecular species in a given electronic–vibrational–rotational excited state according to Equation (5.2) in [48]. The maximum rotational level J_{max} of each excited state is calculated following the rotating Morse oscillator model [49], obtaining $J^B_{max} = 168$, $J^C_{max} = 109$ and $J^a_{max} = 156$. The population of each electronic–vibrational–rotational excited state is calculated from the obtained energies by following a Boltzmann distribution, where the vibrational and the rotational temperature are similar to the gas temperature (T_g). Following laboratory measurements, we introduce a certain degree of thermal non-equilibrium by assuming that the electron temperature can vary between T_{gas} and $2 \times T_{gas}$ [14].

The number density of atoms and ions in the upper energy level i, N_i, is calculated as

$$N_i = (Ng_i/Z(T_g))exp(\epsilon_i/k_B T_g), \quad (1)$$

where k_B is the Boltzmann constant, T_g is the gas temperature, N is the total number density of atoms/ions of each considered species (N I, O I, H I, ...), $Z(T_g)$ is the corresponding partition function, g_i are the statistical weights of level i and ϵ_i is the excitation energy of the level i. The optical emission intensity of a transition from level i to level j is written as [16]

$$I_{ij} = \frac{1}{4\pi} h\nu_{ij} A_{ij} N_i, \quad (2)$$

where h is the Planck's constant, ν_{ij} is the frequency of the emitted photon and A_{ij} is the Einstein coefficient of observed transitions taken from the National Institute of Standard and Technology (NIST) database [47] for the case of the atom and ions, and from [46] in the case of the molecular N_2. The spectra broadening is calculated by combining the instrument, Doppler and Stark broadening contributions following [14]. The instrument broadening is assumed to be 0.42 nm for visualization purposes.

The uncertainty in the calculated spectra is influenced by the accuracy of the tabulated atomic and ionic transitions of the NIST database [47]. In general, the Einstein coefficients of the observed atomic lines are tabulated with an accuracy of $C+$ or better (meaning that the uncertainty is lower than 18%). However, the accuracy of ionic transitions ranges between $C+$ and D level (50%). As the transitions of ions dominate the most energetic part of the spectra, we expect that the uncertainty of the calculated spectra is higher at lower wavelengths, especially in the interval of wavelengths contributing to the photometer PH2.

The calculation of the observed spectra is performed by estimating the atmospheric absorption using the software MODTRAN 5 [50]. MODTRAN 5 does not include the molecular absorption by ozone [51] and by the Schumann-Runge band of molecular oxygen [52] below 200 nm, which can significantly affect the optical signal detected by the photometer PH2 of ASIM-MMIA in the vacuum UV range (180–230 nm). Therefore, we calculate the molecular absorption by ozone and by the Schumann-Runge band of molecular oxygen following [40]. We assume that the angle between the observation path and the vertical is 20°.

2.3.2. Estimation of the Gas and Electron Temperature

The photometers of ASIM-MMIA provide measurements of the optical signal emitted by exposed lightning channels (see Table 1). The main target of photometers PH1 and PH3 are lightning discharges, while TLEs can also contribute to the photometer PH2 [31]. Therefore, we use the measurements of PH1 and PH3 to estimate the gas and electron

temperature. We plot in Figure 1 the theoretical ratio between the photometers PH1 and PH3 for different gas and electron temperatures, assuming that the source is located at a 15 km altitude. The dashed lines correspond to the lower and the upper values of the observed ratios in the three studied events. Figure 1 shows that the ratio of PH1 and PH3 does not provide enough information to estimate the gas and the electron temperatures of the lightning channel. Instead of using the ratio of the photometers as a diagnostic parameter, we use the absolute photon fluxes reported by PH1 and PH3. The measured absolute photon fluxes depend on the volume of the emitting lightning channel and on the altitude of the source. The visible (projected) length of each exposed lightning channel is estimated from the camera recordings for each event by counting all the contiguous pixels with a photon flux value larger than the 90% of the background. Note that the measured length is not the real length of the emerged lightning channel but a projected one onto the camera sensor. We found that those lengths are 2.4 km (event 1 over Peru), 3.2 km (event 2 over Angola) and 8.0 km (event 3 over the Phillipines). The radius of the discharge is assumed to be about 4 cm based on the results of electrodynamical simulations of lightning channels in the scale of tens of microseconds (the sampling frequency of ASIM-MMIA photometers is 100 kHz) [53,54]. Finally, the altitude of the exposed channel is assumed to be similar to the CTH provided by satellites.

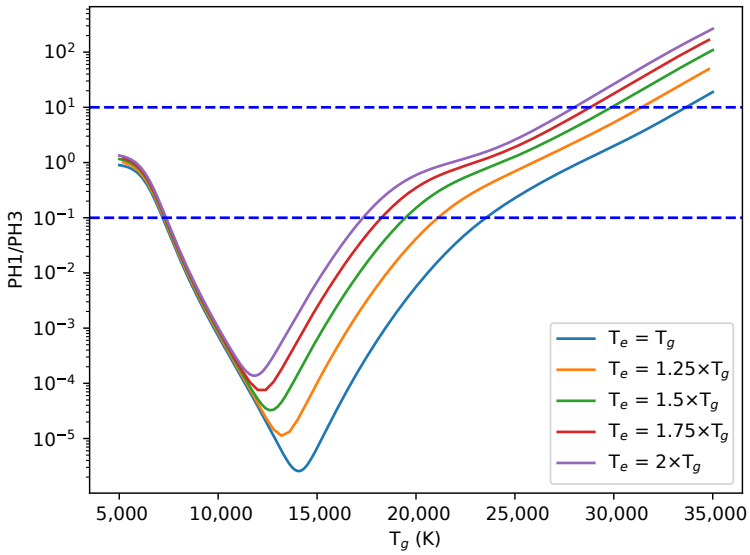

Figure 1. Estimated ratio between the ASIM-MMIA photometers PH1 and PH3 for different gas temperature (T_g) and electron temperature (T_e), assuming that the source is located at 15 km altitude. The blue horizontal dashed lines represent the range of PH1/PH3 values resulting from observations.

The assumptions of the length, radius and altitude of the exposed lightning channel allow us to calculate the synthetic spectra able to reproduce the recordings of PH1 and PH3. To do that, we generate 61,721 synthetic spectra with T_g ranging between 1000 K and 35,000 K and T_e ranging between T_g and $2 \times T_g$ with a temperature step of 100 K. For each event, we search for the pair of T_g and T_e that reproduces the light curves recorded by PH1 and PH3 at the level of each photometer count.

3. Results

3.1. Events

ASIM-MMIA measurements of the three analyzed events are shown in Figure 2. The first event occurred on the 12 November 2018 at 01:14:01.196549 (UTC). The coordinates of this event were about 8.9°S latitude and 75.1°W longitude near Peru. According to the Cloud Top Height (CTH) product derived from GOES-16, the CTH was 12.3 km. The optical signature of this event spread in three frames, while the exposed lightning channel

appears only in the third frame exhibiting a projected length of ∼2 km. The main stroke is detected by the three photometers, including a significant near UV signal measured by PH2. The optical signal measured by the photometer PH2 did not correspond with the typical signal emitted by elves [55]. However, we can not completely discard that it was emitted by other types of TLE. The measurements of the cameras CHU1 and CHU2 suggest the presence of an exposed lightning channel.

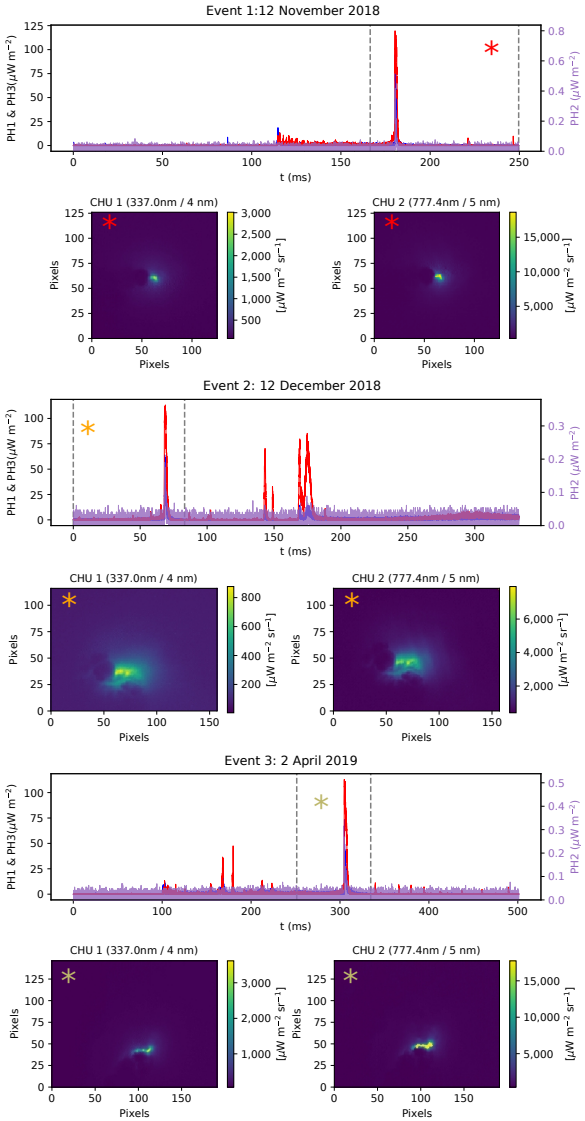

Figure 2. Photometer and camera measurements of the three studied events. The dashed lines (with an asterisk in between) indicate the frame of the main stroke for each event. The images from the cameras (over Peru (event 1), Angola (event 2) and the Phillipines (event 3)) correspond to the frame containing the main stroke. Note that the scale of PH2 is much smaller than that of PH1 and PH3.

The second event took place on the 12 December 2018 at 19:49:32.641714 (UTC) with an estimated exposed channel length of ∼3 km. The coordinates of this event were about 6.5°S latitude and 15.2°E longitude near Angola. The CTH product derived from Meteosat Second Generation (MSG) indicates a CTH of 14.8 km. As in the previous case, the main stroke is simultaneously detected by the three photometers and the optical signal of the PH2 photometer does not indicate the presence of an elve. The optical signal measured by ASIM-MMIA cameras CHU1 and CHU2 suggests the presence of an exposed lightning channel. However, the signal is more diffuse than in the previous case, indicating the possible influence of thin clouds in the scattering of the emitted light.

The third event was detected on the 2 April 2019 at 14:42:17.251059 (UTC) over the Phillipines. The estimated exposed projected channel length is ∼8 km. The approximate coordinates of these events are 4.6°N latitude and 143.2°E longitude, while the CTH derived from the Himawari-8 satellite is at a 15 km altitude. The main stroke took place in the fifth frame and was detected by the three photometers. The optical signal reported by the photometer PH2 does not indicate the presence of an elve. The cameras clearly show the presence of an exposed lightning channel.

3.2. Analysis of ASIM-MMIA Measurements

The analysis of the photometer measurements of the three events is shown in Figure 3. The first, the second and the third rows are a zoom of the main strokes shown in Figure 2 and the ratio between PH1 and PH3. We have subtracted the averaged value of the signal in each frame to reduce the background noise before applying the spectroscopic diagnostic method. The zoomed photometer measurements of event 1 show that the onset of the main stroke was preceded by an isolated increase in the signal of photometer PH3, indicating the possible presence of a leader before the return stroke. The noise in the signal of the photometers PH1 and PH2 suggests that event 2 over Angola was more affected by cloud scattering than events 1 and 3. We obtain a risetime for the blue signal of the event 1 of 0.03 ms, while for events 2 and 3 we obtain 0.27 ms and 0.16 ms, respectively. These risetimes have been derived as the time the signal takes to increase from the 10% to the 90% levels. The differences observed in the risetimes and in the peak optical intensities also indicate that the event 2 could have been more affected by cloud scattering than the other events. The longer trail of the blue signal of the event 3 suggests a longer non-exposed portion of the lightning channel in comparison with the other events. The obtained ratios between PH1 and PH3 indicate that the blue signal was larger than the red signal only during the onset of the main stroke of event 1.

The fourth and the fifth rows of Figure 3 show the derived gas and electron temperature, respectively. The temperatures are only calculated if the signals measured by the photometers PH1 and PH3 are at least 3 times above their minimum values in order to prevent an estimation of the temperature at noise level. For the sake of clarity, the curves have been smoothed by applying a moving average box within 10 counts. The calculated temperatures are reliable only for the photometer counts where the PH1/PH3 ratio is significantly different from the noise. As a consequence, the derived temperatures of the advancing leader of event 1 are not considered reliable. The obtained gas temperature ranges between ∼20,000 K and ∼30,000 K, while the electron temperature can reach up to ∼40,000 K. The gas temperature does not vary considerably during the evolution of the main pulse, while the electron temperature tends to decrease.

The photons reaching the sensor in the first counts (tens of microseconds) are probably the photons emitted by the exposed lightning channel [40]. However, the tail of the main pulses is likely influenced by scattered photons emitted inside or below clouds. Thus, we consider that the gas and electron temperatures in the exposed lightning channel are those corresponding to the rise of the main pulses. The gas and the electron temperature derived during the decay of the pulses can be considered as effective temperatures influenced by photons emitted at different times and do not provide any evident information about the plasma in the lightning channel. For the event 1, we obtain T_g = 21,800 K and T_e = 35,000 K at the peak of the blue signal (time when the risetime is reached). For the event 2, we obtain T_g = 21,400 K and T_e = 36,600 K. Finally, we obtain T_g = 22,800 K and T_e = 34,400 K for the event 3. Therefore, the ratio between the electron and the gas temperatures ranges between 1.5 and 1.7.

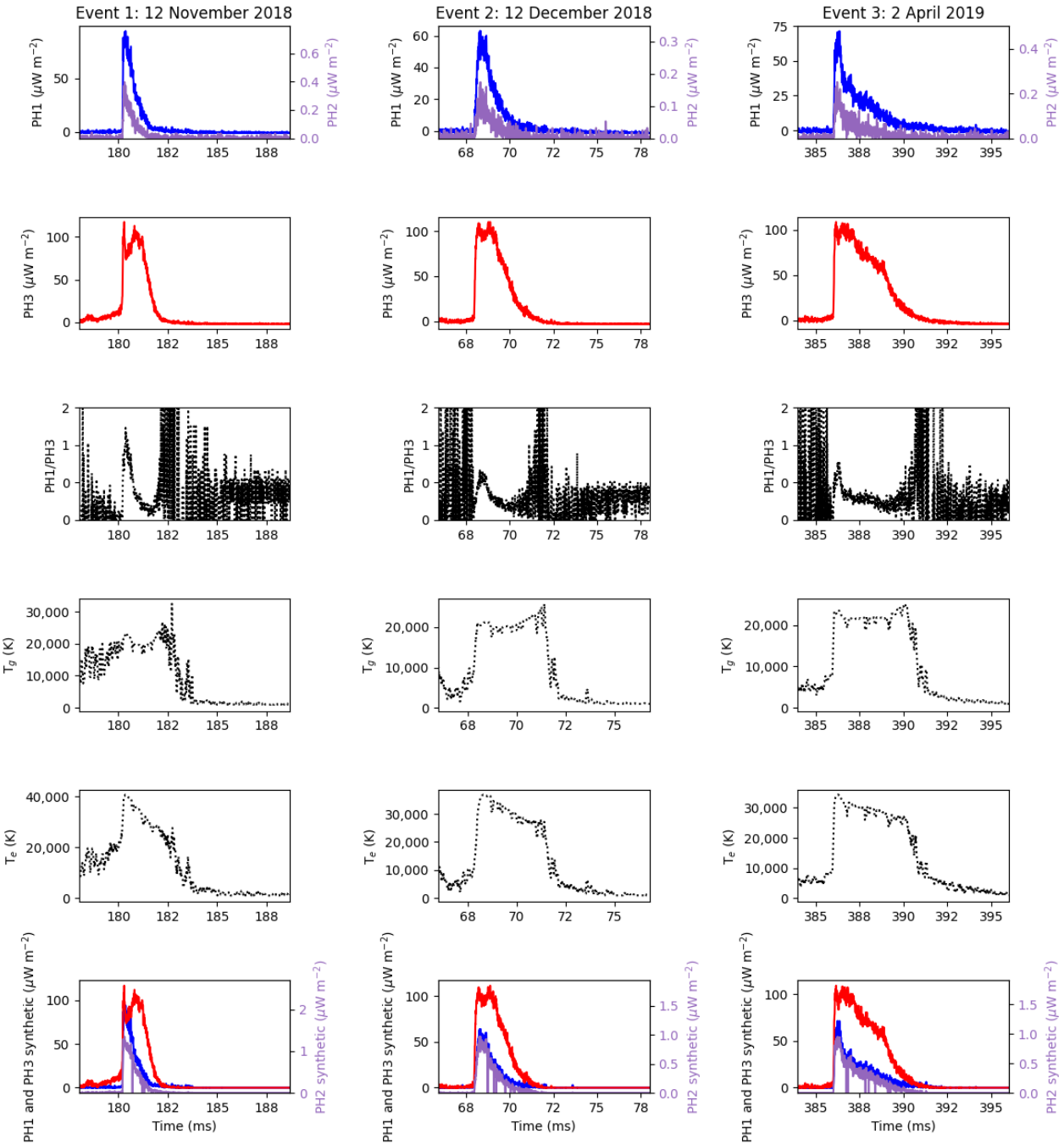

Figure 3. First and second rows: Zoomed photometer measurements (PH1: Blue line, PH2: Purple line, PH3: Red line) for the three analyzed events. **Third row**: Ratio between PH1 and PH3. **Fourth and fifth rows**: Derived gas and electron temperatures. **Sixth row**: Theoretical photometer measurements from the derived gas and electron temperatures.

The sixth row of Figure 3 shows the theoretical photometer measurements recovered from the calculated gas and electron temperatures at each photometer count. The obtained PH1 and PH3 theoretical signals are in agreement with the measured signals. However, the obtained theoretical signal of PH2 is about a factor 3 to 4 larger than the measured signal. The disagreement between the theoretical and the measured PH2 signal could be due to the large uncertainty in the Einstein coefficients of ionic transitions, the uncertainty in the calculation of the absorption of the atmosphere at extreme low wavelengths and/or to a possible deviation of the plasma with respect to the equilibrium concentration of species.

Figure 4 shows the theoretical contribution to the three photometers of ASIM-MMIA for the three selected events versus the gas temperature assuming that T_e/T_g = 1.6, that is, the ratio between the electron and the gas temperatures averaged over all the events. The contribution of the optical emissions to the photometer PH1 and PH3 (left panels of Figure 4) are larger for events at a lower altitude. The reason is that the air density is larger at lower altitude and the total number of photons emitted per cubic meter is higher. On the contrary, the contribution of the exposed lightning channel to the photometer PH2 is larger for emitting sources located at higher altitudes. This is a consequence of the high atmospheric absorption for the wavelength interval 180–230 nm.

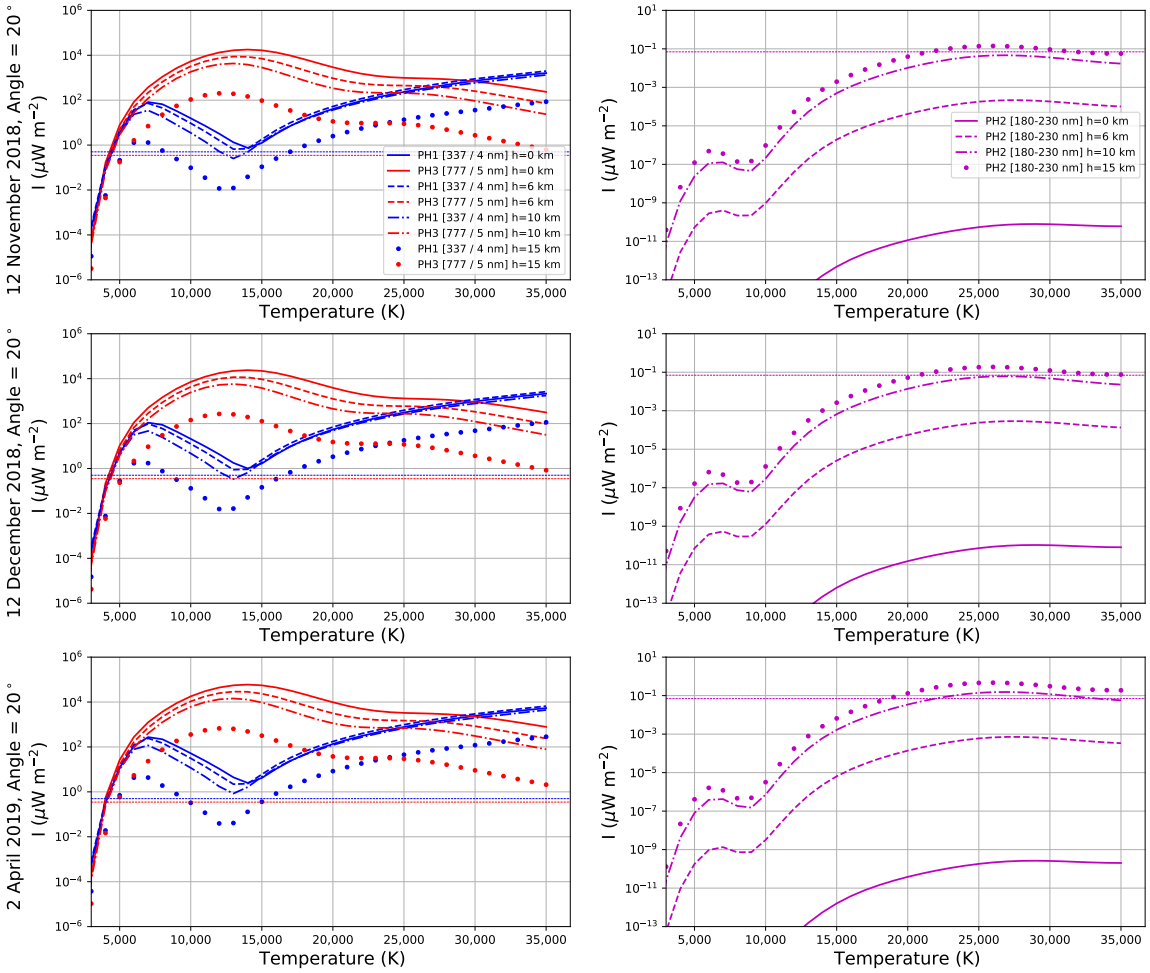

Figure 4. Theoretical contributions to the three photometers of ASIM-MMIA for the three selected events located at four possible source altitudes (0 km, 6 km, 10 km and 15 km) and assuming that $T_e = 1.6 \times T_g$. The line of sight forms 20° with respect to the vertical direction. The horizontal lines (red, blue and purple) represent the thresholds for each photometer of ASIM-MMIA. Note that the atmosphere absorption from the source to the detector (ASIM-MMIA) is already considered in these plots.

The contribution of the emerged (from the cloud) lightning channel to the photometer PH1 (337/4 nm) between ∼3000 K and ∼14,000 K is dominated by molecular optical emissions from the electronic–vibrational–rotational excited states of N_2. Molecular N_2 dissociation becomes evident at ∼6000 K and, consequently, N_2 337 nm optical emissions smoothly decline from ∼6000 K to ∼14,000 K. The signal of the photometer PH1 grows again for T_g > 14,000 K as a consequence of an increase in the population of oxygen and nitrogen ions O II, N II (see Table 1).

The synthetic optical signal of the photometer PH3 (777.4/5 nm) increases with the temperature up to $T_g \sim 14{,}000$ K, but it decreases for higher gas temperatures. As shown in Table 1, the most important species contributing to PH3 is atomic oxygen O I, which concentration decreases from ∼14,000 K as a consequence of the higher thermal ionization of the air.

According to Figure 4, molecular emissions within the LBH band emitted by the exposed lightning channel are generally not detectable by photometer PH2 (180–230 nm). The contribution of the exposed lightning channel to PH2 is only detectable for gas temperature above ∼18,000–20,000 K that activate optical emissions from ionized species, such as O II, N II and N III (see Table 1). In addition, Figure 4 shows that the contribution of the thermal plasma of the lightning stroke to PH2 can only be detected if the altitude of the emitting source is above 10 km altitude. Thus, the optical signal detected by PH2 may be less influenced by scattered photons than the optical signals reported by PH1 and PH3. This is in agreement with the photometer measurements in Figure 3, showing that the total duration of the pulse detected by PH2 is shorter than the total duration reported by PH1 and PH3.

The synthetic spectra (emitted and observed) of the three analyzed events are shown in Figures 5 and 6 in linear and logarithmic scale, respectively. These spectra have been calculated by using the pair T_g and T_e obtained for each event and assuming that the altitude of the source is 15 km. An inspection to the spectra at wavelengths below 300 nm indicates that the optical radiation at low wavelengths is highly absorbed by the atmosphere. However, some lines can still contribute to the photometer PH2. The spectral lines contributing to the photometers PH1 and PH3 are among the most important lines in the emitted and the observed spectra. Nevertheless, Figures 5 and 6 clearly show that a significant amount of radiated power can also be received in the range of wavelengths between 350 nm and 700 nm.

Figure 7 shows the radiated power of a heated lightning stroke channel at ∼15 km assuming a channel radius of 4 cm and $T_e/T_g = 1.6$. Three different regimes can be observed in Figure 7 depending on the gas temperature of the lightning channel. The radiated power is dominated by ultraviolet (100–380 nm) optical emissions below ∼17,000 K, mainly due to the neutral nitrogen doublet emitting at 174.272 nm and 174.525 nm (see below). Between ∼17,000 K and ∼27,000 K, the main contribution to the source radiated power is from atomic emissions in the visible-near infrarred (380–780 nm) spectral range. Finally, ionic emissions in the ultraviolet represent the main contribution to the radiated power above ∼27,000 K. The obtained fraction of optical power radiated in the visible-near infrarred varies between 5% and 80%, which is slightly above the estimations of [56] and references therein ranging between 3% and 49%.

Let us now analyze the optical signal reported by the ASIM-MMIA cameras, shown in the first and the second rows of Figure 8. We have applied the previously described diagnostic method to estimate the gas and the electron temperatures in each of the pixels of the ASIM-MMIA cameras. Firstly, we have aligned the images of the two cameras and have inspected the ratio between CHU1 and CHU2, shown in the third row of Figure 8. Finally, we have estimated the map of gas temperatures (fourth row) and electron temperatures (fifth row) by assuming that the radius of the discharge is 80 cm. This radius is extracted from electrodynamical simulations of lightning stroke channels reported in (Figures 14 and 15 [53]), where it is shown that the radius of a lightning stroke channel with a high concentration of electrons between 0.01 s (10 ms) and 1 s after the onset of the lightning discharge ranges between 50 cm and 110 cm.

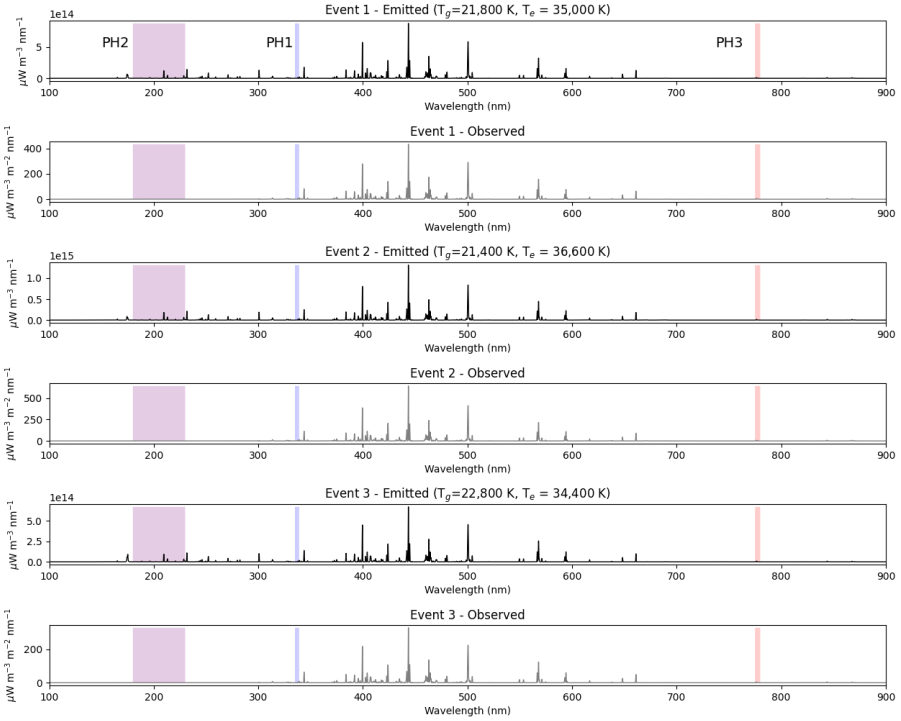

Figure 5. Synthetic emitted and observed spectra (linear scale) for the three considered events assuming a source altitude of 15 km. The blue, purple and red shadows correspond to the photometer bands of PH1, PH2 and PH3, respectively. The m^{-3} unit in the emission intensity indicates that we have not multiplied the emission intensity by the volume of the exposed lightning stroke channel.

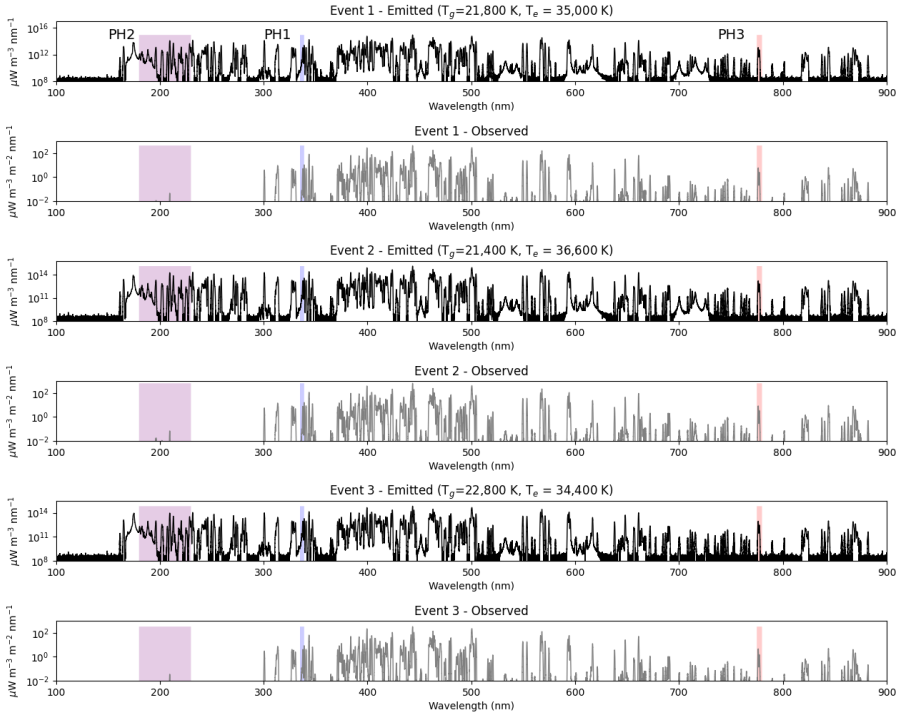

Figure 6. Synthetic emitted and observed spectra (logarithmic scale) for the three considered events assuming a source altitude of 15 km. The blue, purple and red shadows correspond to the photometer bands of PH1, PH2 and PH3, respectively. The m^{-3} unit in the emission intensity indicates that we have not multiplied the emission intensity by the volume of the exposed lightning stroke channel.

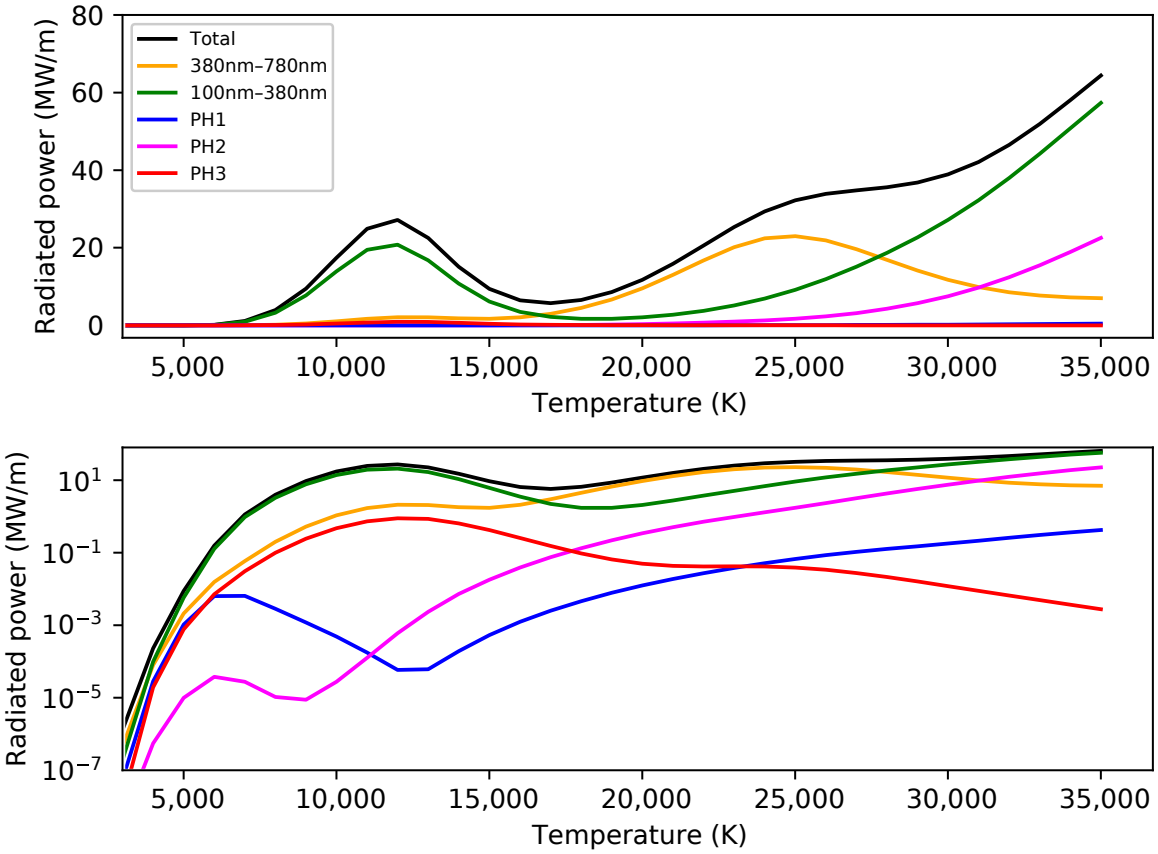

Figure 7. Source radiated power (MW/m) in the ultraviolet (100–380 nm), visible-near infrarred (380–780 nm), and within the PH1, PH2 and PH3 ASIM-MMIA photometer spectral ranges as a function of the gas temperature assuming that $T_e/T_g = 1.6$. Note that PH1, PH2 and PH3 cover the spectral ranges in 337 $\pm$ 2 nm, 180–230 nm and 777.4 $\pm$ 2.5 nm, respectively.

The gas and electron temperatures obtained from the signals reported by the cameras are significantly lower than the values derived from the photometer measurements. This disagreement is explained by the different integration times of photometers and cameras. The sampling frequency of the photometers is 10 microseconds, while it is 83 ms for the cameras. Thus, the photons received by the photometers during the first counts are mainly emitted at the onset of the exposed lightning stroke channel, while in the case of the cameras the photons received in a frame are emitted by the complete discharge and at different times, possibly during the cooling phase. As a consequence, the camera obtained gas and electron temperatures are lower than those resulting from the analysis of the light curves recorded by the ASIM-MMIA photometers.

The maps shown in Figure 8 for the gas and the electron temperatures of events 1 and 3 are in agreement with the spatial structure of the emerged lightning stroke channels. However, the maps for the calculated gas and the electron temperatures of event 2 (center column in Figure 8) do not reproduce the spatial structure of the emerged lightning channel. The reason for this disagreement in the event 2 is that the exposed lightning channel is more affected by cloud scattering than in the cases of events 1 and 3. This was already pointed out in the analysis of the photometer measurements.

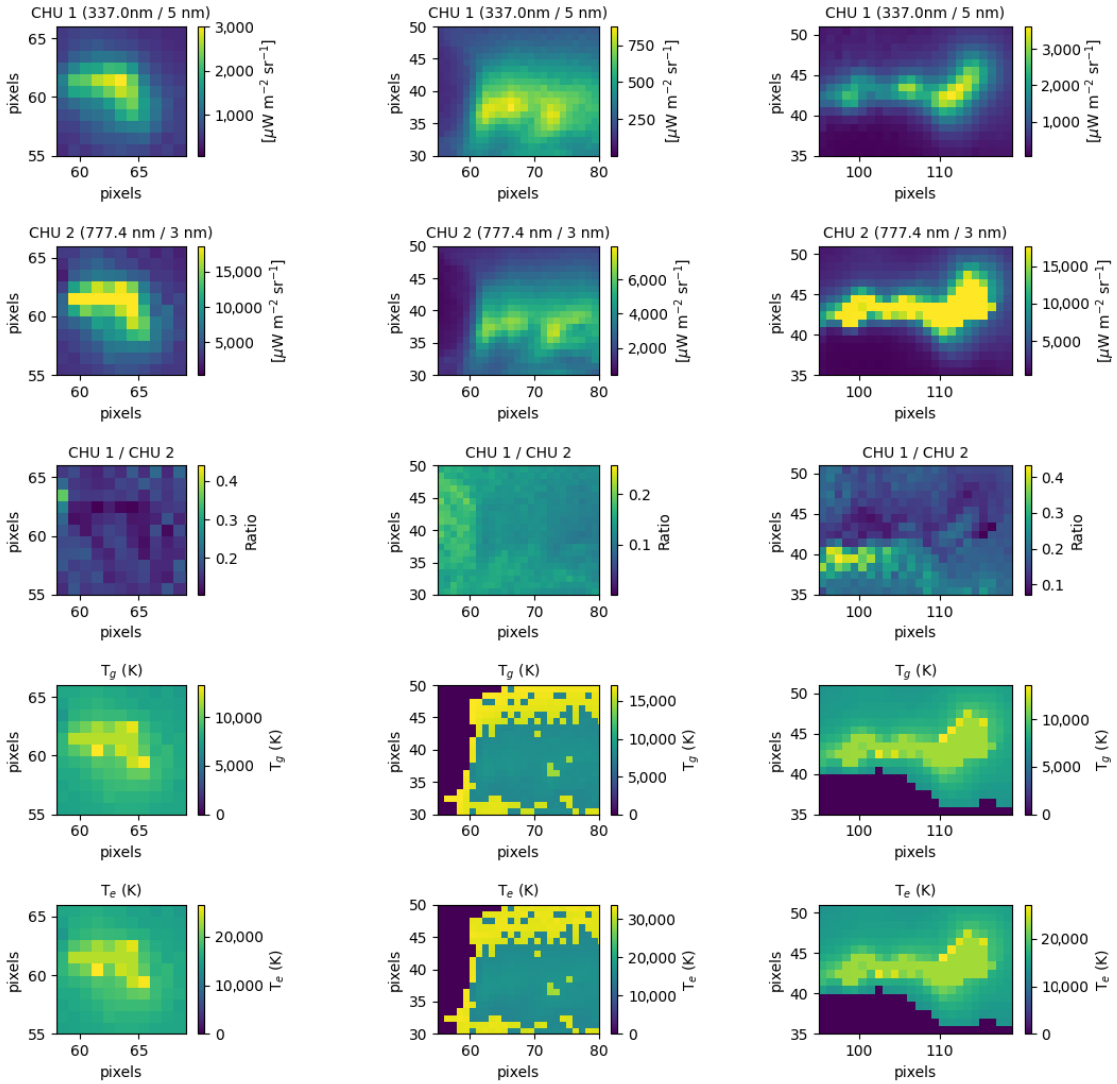

Figure 8. First and second rows: Zoomed camera measurements for the three analyzed events. **Third row**: Ratio between CHU1 and CHU2. **Fourth and fifth rows**: Derived maps for the gas and electron temperatures.

4. Discussion and Conclusions

Three emerged lightning stroke channels taking place in three different thunderstorms have been selected by using the high spatial resolution cameras of ASIM-MMIA. We have developed a spectroscopic diagnostic method to estimate the gas and the electron temperatures in the exposed lightning channels detected by ASIM-MMIA photometers and cameras. The high sampling rate of the ASIM-MMIA photometers represents a unique opportunity to derive from space some parameters of the air plasma produced within a lightning stroke. Our diagnostic method relies on the comparison between photometer measurements and synthetic spectra of the hot lightning stroke calculated at different gas and electron temperatures. We have assumed that the optical emissions from emerged lightning stroke channels are not influenced by optical emissions from streamers. The obtained gas temperatures for the three events are in agreement with electrodynamical simulations and laboratory measurements on the temporal scale of tens of microseconds. In addition, the derived electron temperatures are higher than the gas temperatures, indicating that the air plasma formed by the lightning stroke is not in thermal equilibrium or that photometer measurements could be influenced by optical emissions from streamers.

Previous results [57–59] for return strokes in rocket-triggered lightning and laboratory arc discharges demonstrate that the relation between the instantaneous current and the instantaneous luminosity can be divided into three stages: the initial rising stage in which both the current and the luminosity rise rapidly, the initial fast decay stage in which the luminosity decays fast from the peak, whereas the current may remain constant or increase slightly and then slowly decays, and the later slow decay stage in which both the luminosity and the current decrease slowly. Recent high speed spectroscopy of rocket-triggered lightning [12,13] and lightning-like discharges [14,15] indicate that single and doubly ionized atomic ions are present at submicrosecond time scales and during the very first microseconds, which is an indication of high temperatures well above ∼27,000 K. Thus, according to Figure 7, the initial rising stage of a lightning return stroke produces radiated power in the VIS (380–780 nm) but mainly in the UV (100–380 nm) including ionic emissions within the PH1 and PH2 ranges. Therefore, most of the UV optical emissions that dominate above ∼27,000 K come from ionic species formed during the early (initial rising) stage when the gas temperature reaches very high values. As the lightning stroke channel cools down, VIS radiated power grows and prevails over UV between ∼27,000 K and ∼17,000 K. At lower temperatures between ∼17,000 K and ∼6000 K, UV emissions (excluding molecular and ionic emissions in PH1 and PH2) dominate (over visible emissions) due to the neutral nitrogen doublet emitting at 174.272 nm and 174.525 nm. However, these lines are absorbed by the O_2 Schumann-Runge bands and continuum in their way to ASIM-MMIA in the ISS. The molecular N_2 SPS emissions in 337.0 nm and N_2 LBH emissions in 180–230 nm within, respectively, PH1 and PH2 only start to grow from ∼12,000 K (for PH1) and ∼8000 K (for PH2), and reach their maxima at ∼6000 K. Below ∼6000 K molecular N_2 SPS 337 nm emissions in PH1 compete with 777.4 nm emissions from neutral oxygen. Most VIS (380–780 nm) radiation between ∼3000 K and ∼12,000 K is due to 777.4 nm. However, 777.4 nm near infrarred radiation from lightning strokes steadily decreases from ∼12,000 K to 35,000 K. Therefore, we consider that Figure 7 can serve as an approximate guidance to determine the temporal stages of lightning stroke channels, whether rising or decaying.

The detailed synthetic spectra calculated in this work and the comparison with the ASIM-MMIA fast multiwavelength photometric observations demonstrate that: (i) early stage (high temperature $>$ 20,000 K) emerged lightning strokes at high altitude can contribute to the optical signals measured by the PH2 photometer (180–230 nm); (ii) intermediate stage (mid temperatures, 6000–21,000 K) emerged lightning strokes can produce 777.4 nm near-infrarred radiation (observable by PH3) exhibiting higher intensity than PH1 observable N_2 SPS between ∼6000 K and ∼8000 K, and then ion optical emissions (336.734 nm and 337.714 nm) between ∼16,000 K and ∼21,000 K; (iii) from ∼16,000 K to 35,000 K, neutral oxygen 777.4 nm radiation and ion emissions at 336.734 nm and 337.714 nm can be simultaneoulsy observed, but 777.4 nm dominates only between ∼16,000 K and ∼21,000 K; (iv) the availability of detections with a narrow 0.5 nm gap filtered photometer (336.75–337.25 nm), with the same or better sensitivity than PH1 in ASIM-MMIA but with a central wavelength at exactly 337.0 nm (the strongest N_2 SPS transition), would give access to the late stage of lightning strokes (emerged or not) when temperatures are between 8000 K and 5000 K (or lower for a photometer with better sensitivity than PH1 in ASIM-MMIA) when the production of nitrogen oxides (NO_x) and hydroxyl radicals (OH) maximizes. Thus, we conclude that multiwavelength sensors onboard future space platforms could be a useful tool to diagnose the temporal thermal non-equilibrium dynamics of lightning strokes that could inform about the chemical activity regime of the observed lightning strokes.

Author Contributions: Conceptualization, F.J.P.-I. and F.J.G.-V.; methodology, F.J.P.-I. and F.J.G.-V.; software, F.J.P.-I.; validation, F.J.P.-I., F.J.G.-V. and M.P.-V.; formal analysis, F.J.P.-I. and F.J.G.-V.; investigation, F.J.P.-I., F.J.G.-V., M.P.-V., T.N., O.C., V.R. and N.Ø.; resources, F.J.G.-V.; data curation, F.J.P.-I., F.J.G.-V., T.N. and O.C.; writing—original draft preparation, F.J.P.-I. and F.J.G.-V.; writing—review and editing, F.J.P.-I., F.J.G.-V., M.P.-V., T.N., O.C., V.R. and N.Ø.; project administration, F.J.P.-I.

and F.J.G.-V.; funding acquisition, F.J.G.-V. All authors have read and agreed to the published version of the manuscript.

Funding: This research was funded by the Spanish Ministry of Science and Innovation, under projects PID2019-109269RB-C43 and FEDER program. F.J.P.-I. acknowledges the sponsorship provided by Junta de Andalucia under grant number POSTDOC-21-00052. F.J.P.-I., F.J.G.-V. and M.P.-V. acknowledge financial support from the State Agency for Research of the Spanish MCIU through the 'Center of Excellence Severo Ochoa' award for the Instituto de Astrofisica de Andalucia (SEV-2017-0709). The APC was funded by the project PID2019-109269RB-C43.

Informed Consent Statement: Not applicable.

Data Availability Statement: ASIM level 1 data are proprietary and cannot be publicly released at this stage. Interested parties should direct their request to the ASIM Facility Science Team (FST). ASIM data request can be submitted through: https://asdc.space.dtu.dk (accessed on 7 April 2022) by sending a message to the electronic address asdc@space.dtu.dk.

Acknowledgments: ASIM is a mission of the ESA SciSpace program for the scientific utilization of the ISS and non-ISS space exploration platforms and space environment analogs. It is funded by ESA and national contributions through contracts with TERMA and the Technical University of Denmark (DTU) in Denmark, the University of Bergen (UB) in Norway and the University of Valencia (UV) in Spain.

Conflicts of Interest: The authors declare no conflict of interest. The funders had no role in the design of the study; in the collection, analyses, or interpretation of data; in the writing of the manuscript, or in the decision to publish the results.

Abbreviations

The following abbreviations are used in this manuscript:

ASIM	Atmosphere Space Interaction Monitor
CCD	Charge-Coupled Device
CHU	Camera Head Units
CTH	Cloud Top Height
FPS	First Positive System
FUV	Far UltraViolet
ISUAL	Imager of Sprites and Upper Atmospheric Lightning
LBH	Lyman Birge Hopfield
LIS	Lightning Imaging Sensor
LTE	Local Thermal Equilibrium
MMIA	Modular Multispectral Imaging Array
MSG	Meteosat Second Generation
OTD	Optical Transient Detector
PH	Photometer
SPS	Second Positive System
T_e	Electron temperature
T_g	Gas temperature
TLEs	Transient Luminous Events
TRMM	Tropical Rainfall Measuring Mission
UTC	Universal Time Coordinated
UV	UltraViolet

References

1. Christian, H.J.; Blakeslee, R.J.; Boccippio, D.J.; Boeck, W.L.; Buechler, D.E.; Driscoll, K.T.; Goodman, S.J.; Hall, J.M.; Koshak, J.M.; Mach, D.M.; et al. Global frequency and distribution of lightning as observed from space by the Optical Transient Detector. *J. Geophys. Res.* **2003**, *108*, ACL 4-1. [CrossRef]
2. Cecil, D.J.; Buechler, D.E.; Blakeslee, R.J. Gridded lightning climatology from TRMM-LIS and OTD: Dataset description. *Atmos. Res.* **2014**, *135*, 404–414. [CrossRef]

3. Blakeslee, R.; Lang, T.; Koshak, W.; Buechler, D.; Gatlin, P.; Mach, D.; Stano, G.; Virts, K.; Walker, T.; Cecil, D.; et al. Three years of the Lightning Imaging Sensor onboard the International Space Station: Expanded Global Coverage and Enhanced Applications. *Earth Space Sci. Open Arch.* **2020**, *35812*, 83. [CrossRef]
4. Walker, T.D. A 21st Century Investigation of the Lightning Spectrum. Ph.D. Thesis, School of Graduate Studies of the University of Alabama in Huntsville, Huntsville, AL, USA, 2015.
5. Beirle, S.; Koshak, W.; Blakeslee, R.; Wagner, T. Global patterns of lightning properties derived by OTD and LIS. *Nat. Hazards Earth Syst. Sci.* **2014**, *14*, 2715–2726. [CrossRef]
6. Marchand, M.; Hilburn, K.; Miller, S.D. Geostationary Lightning Mapper and Earth Networks lightning detection over the contiguous United States and dependence on flash characteristics. *J. Geophys. Res. Atmos.* **2019**, *124*, 11552–11567. [CrossRef]
7. Rudlosky, S.D.; Goodman, S.J.; Virts, K.S.; Bruning, E.C. Initial geostationary lightning mapper observations. *Geophys. Res. Lett.* **2019**, *46*, 1097–1104. [CrossRef]
8. Liu, Y.; Wang, H.; Li, Z.; Wang, Z. A verification of the lightning detection data from FY-4A LMI as compared with ADTD-2. *Atmos. Res.* **2021**, *248*, 105163. [CrossRef]
9. Chang, S.C.; Kuo, C.L.; Lee, L.J.; Chen, A.B.; Su, H.T.; Hsu, R.R.; Frey, H.U.; Mende, S.B.; Takahashi, Y.; Lee, L.C. ISUAL far-ultraviolet events, elves, and lightning current. *J. Geophys. Res. (Space Phys.)* **2010**, *115*, A00E46. [CrossRef]
10. Adachi, T.; Cummer, S.A.; Li, J.; Takahashi, Y.; Hsu, R.R.; Su, H.T.; Chen, A.B.; Mende, S.B.; Frey, H.U. Estimating lightning current moment waveforms from satellite optical measurements. *Geophys. Res. Lett.* **2009**, *36*, *L18808*. [CrossRef]
11. Rakov, V.A.; Uman, M.A. *Lightning Physics and Effects*; Cambridge University Press: Cambridge, UK, 2003.
12. Walker, T.D.; Christian, H.J. Triggered lightning spectroscopy: Part 1. A qualitative analysis. *J. Geophys. Res. Atmos.* **2017**, *122*, 8000–8011. [CrossRef]
13. Walker, T.D.; Christian, H.J. Triggered lightning spectroscopy: 2. A quantitative analysis. *J. Geophys. Res. Atmos.* **2019**, *124*, 3930–3942. [CrossRef]
14. Kieu, N.; Gordillo-Vázquez, F.J.; Passas, M.; Sánchez, J.; Pérez-Invernón, F.J.; Luque, A.; Montanyá, J.; Christian, H. Submicrosecond spectroscopy of lightning-like discharges: Exploring new time regimes. *Geophys. Res. Lett.* **2020**, *47*, e2020GL088755. [CrossRef] [PubMed]
15. Kieu, N.; Gordillo-Vázquez, F.J.; Passas, M.; Sánchez, J.; Pérez-Invernón, F.J. High-speed spectroscopy of lightning-like discharges: Evidence of molecular optical emissions. *J. Geophys. Res. Atmos.* **2021**, *126*, e2021JD035016. [CrossRef]
16. Orville, R.E. Spectrum of the lightning stepped leader. *J. Geophys. Res.* **1968**, *73*, 6999–7008. [CrossRef]
17. Orville, R.E.; Salanave, L.E. Lightning Spectroscopy—Photographic Techniques. *Appl. Opt.* **1970**, *9*, 1775–1781. [CrossRef]
18. Christian, H.; Frost, R.; Gillaspy, P.; Goodman, S.; Vaughan, O., Jr.; Brook, M.; Vonnegut, B.; Orville, R. Observations of optical lightning emissions from above thunderstorms using U-2 aircraft. *Bull. Am. Meteorol. Soc.* **1983**, *64*, 120–123. [CrossRef]
19. Christian, H.; Goodman, S. Optical observations of lightning from a high-altitude airplane. *J. Atmos. Ocean Technol.* **1987**, *4*, 701–711. [CrossRef]
20. Gigosos, M.A.; Gonzalez, M.A.; Cardenoso, V. Computer simulated Balmer alpha, beta and gamma Stark line profiles for non-equilibrium plasmas diagnostics. *Spectrochim. Acta Part B At. Spectrosc.* **2003**, *58*, 1489–1504. [CrossRef]
21. Nikiforov, A.Y.; Leys, C.; Gonzalez, M.; Walsh, J. Electron density measurement in atmospheric pressure plasma jets: Stark broadening of hydrogenated and non-hydrogenated lines. *Plasma Sources Sci. Technol.* **2015**, *24*, 034001. [CrossRef]
22. Prueitt, M.L. The excitation temperature of lightning. *J. Geophys. Res.* **1963**, *68*, 803–811. [CrossRef]
23. Uman, M.A. Determination of lightning temperature. *J. Geophys. Res.* **1969**, *74*, 949–957. [CrossRef]
24. Paris, P.; Aints, M.; Valk, F.; Plank, T.; Haljaste, A.; Kozlov, K.V.; Wagner, H.E. Intensity ratio of spectral bands of nitrogen as a measure of electric field strength in plasmas. *J. Phys. D* **2005**, *38*, 3894. [CrossRef]
25. Šimek, M. Optical diagnostics of streamer discharges in atmospheric gases. *J. Phys. D* **2014**, *47*, 463001. [CrossRef]
26. Hoder, T.; Simek, M.; Bonaventura, Z.; Prukner, V.; Gordillo-Vázquez, F.J. Radially and temporally resolved electric field of positive streamers in air and modelling of the induced plasma chemistry. *Plasma Sources Sci. Technol.* **2016**, *25*, 045021. [CrossRef]
27. Bílek, P.; Obrusnik, A.; Hoder, T.; Šimek, M.; Bonaventura, Z. Electric field determination in air plasmas from intensity ratio of nitrogen spectral bands: II. Reduction of the uncertainty and state-of-the-art model. *Plasma Sources Sci. Technol.* **2018**, *27*, 085012. [CrossRef]
28. Pérez-Invernón, F.J.; Luque, A.; Gordillo-Vazquez, F.J.; Sato, M.; Ushio, T.; Adachi, T.; Chen, A.B. Spectroscopic Diagnostic of Halos and Elves Detected From Space-Based Photometers. *J. Geophys. Res. Atmos.* **2018**, *123*, 12917–12941. [CrossRef]
29. Malagón-Romero, A.; Pérez-Invernón, F.; Luque, A.; Gordillo-Vázquez, F.J. Analysis of the spatial non-uniformity of the electric field in spectroscopic diagnostic methods of atmospheric electricity phenomena. *J. Geophys. Res. Atmos.* **2019**, *124*, 12356–12370. [CrossRef] [PubMed]
30. Neubert, T.; Østgaard, N.; Reglero, V.; Blanc, E.; Chanrion, O.; Oxborrow, C.A.; Orr, A.; Tacconi, M.; Hartnack, O.; Bhanderi, D.D. The ASIM mission on the International Space Station. *Space Sci. Rev.* **2019**, *215*, 26. [CrossRef]
31. Chanrion, O.; Neubert, T.; Rasmussen, I.L.; Stoltze, C.; Tcherniak, D.; Jessen, N.C.; Polny, J.; Brauer, P.; Balling, J.E.; Kristensen, S.S.; et al. The Modular Multispectral Imaging Array (MMIA) of the ASIM payload on the International Space Station. *Space Sci. Rev.* **2019**, *215*, 28. [CrossRef]

32. van der Velde, O.A.; Montanyà, J.; Neubert, T.; Chanrion, O.; Østgaard, N.; Goodman, S.; López, J.A.; Fabró, F.; Reglero, V. Comparison of high-speed optical observations of a lightning flash from space and the ground. *Earth Space Sci.* **2020**, *7*, e2020EA001249. [CrossRef]
33. Montanyà, J.; López, J.A.; Morales Rodriguez, C.A.; van der Velde, O.A.; Fabró, F.; Pineda, N.; Navarro-González, J.; Reglero, V.; Neubert, T.; Chanrion, O.; et al. A Simultaneous Observation of Lightning by ASIM, Colombia-Lightning Mapping Array, GLM, and ISS-LIS. *J. Geophys. Res. Atmos.* **2021**, *126*, e2020JD033735. [CrossRef]
34. López, J.A.; Montanyà, J.; van der Velde, O.; Romero, D.; Gordillo-Vázquez, F.J.; Pérez-Invernón, F.J.; Luque, A.; Morales, C.; Neubert, T.; Rison, W.; et al. Initiation of lightning flashes simultaneously observed from space and the ground: Narrow bipolar events. *Atmos. Res.* **2021**, *268*, 105981. [CrossRef]
35. Soler, S.; Pérez-Invernón, F.J.; Gordillo-Vázquez, F.J.; Luque, A.; Li, D.; Malagón-Romero, A.; Neubert, T.; Chanrion, O.; Reglero, V.; Navarro-Gonzalez, J.; et al. Blue optical observations of narrow bipolar events by ASIM suggest corona streamer activity in thunderstorms. *J. Geophys. Res. Atmos.* **2020**, *125*, e2020JD032708. [CrossRef]
36. Neubert, T.; Østgaard, N.; Reglero, V.; Chanrion, O.; Heumesser, M.; Dimitriadou, K.; Christiansen, F.; Budtz-Jørgensen, C.; Kuvvetli, I.; Rasmussen, I.L.; et al. A terrestrial gamma-ray flash and ionospheric ultraviolet emissions powered by lightning. *Science* **2020**, *367*, 183–186. [CrossRef] [PubMed]
37. Soler, S.; Gordillo-Vázquez, F.J.; Pérez-Invernón, F.; Luque, A.; Li, D.; Neubert, T.; Chanrion, O.; Reglero, V.; Navarro-González, J.; Østgaard, N. Global frequency and geographical distribution of nighttime streamer corona discharges (BLUEs) in thunderclouds. *Geophys. Res. Lett.* **2021**, *48*, e2021GL094657. [CrossRef]
38. Liu, F.; Lu, G.; Neubert, T.; Lei, J.; Chanrion, O.; Østgaard, N.; Li, D.; Luque, A.; Gordillo-Vázquez, F.J.; Reglero, V.; et al. Optical emissions associated with narrow bipolar events from thunderstorm clouds penetrating into the stratosphere. *Nat. Commun.* **2021**, *12*, 6631. [CrossRef]
39. Neubert, T.; Chanrion, O.; Heumesser, M.; Dimitriadou, K.; Husbjerg, L.; Rasmussen, I.L.; Østgaard, N.; Reglero, V. Observation of the onset of a blue jet into the stratosphere. *Nature* **2021**, *589*, 371–375. [CrossRef]
40. Luque, A.; Gordillo-Vázquez, F.J.; Li, D.; Malagón-Romero, A.; Pérez-Invernón, F.J.; Schmalzried, A.; Soler, S.; Chanrion, O.; Heumesser, M.; Neubert, T.; et al. Modeling lightning observations from space-based platforms (CloudScat. jl 1.0). *Geosci. Model Dev.* **2020**, *13*, 5549–5566. [CrossRef]
41. Schmetz, J.; Pili, P.; Tjemkes, S.; Just, D.; Kerkmann, J.; Rota, S.; Ratier, A. An introduction to Meteosat second generation (MSG). *Bull. Am. Meteorol. Soc* **2002**, *83*, 977–992. [CrossRef]
42. Liu, Q.; Li, Y.; Yu, M.; Chiu, L.S.; Hao, X.; Duffy, D.Q.; Yang, C. Daytime rainy cloud detection and convective precipitation delineation based on a deep neural Network method using GOES-16 ABI images. *Remote Sens.* **2019**, *11*, 2555. [CrossRef]
43. Huang, Y.; Siems, S.; Manton, M.; Protat, A.; Majewski, L.; Nguyen, H. Evaluating Himawari-8 cloud products using shipborne and CALIPSO observations: Cloud-top height and cloud-top temperature. *J. Atmos. Ocean Technol.* **2019**, *36*, 2327–2347. [CrossRef]
44. Godin, D.; Trépanier, J. A robust and efficient method for the computation of equilibrium composition in gaseous mixtures. *Plasma Chem. Plasma Process.* **2004**, *24*, 447–473. [CrossRef]
45. Teulet, P.; Gonzalez, J.; Mercado-Cabrera, A.; Cressault, Y.; Gleizes, A. One-dimensional hydro-kinetic modelling of the decaying arc in air–PA66–copper mixtures: I. Chemical kinetics, thermodynamics, transport and radiative properties. *J. Phys. D* **2009**, *42*, 175201. [CrossRef]
46. Gilmore, F.R.; Laher, R.R.; Espy, P.J. Franck-Condon Factors, r-Centroids, Electronic Transition Moments, and Einstein Coefficients for Many Nitrogen and Oxygen Band Systems. *J. Phys. Chem. Ref. Data* **1992**, *21*, 1005. [CrossRef]
47. Ralchenko, Y.; Jou, F.C.; Kelleher, D.E.; Kramida, A.; Musgrove, A.; Reader, J.; Wiese, W.L.; Olsen, K.J. Nist Atomic Spectra Database (Version 3.1.0). 2006. Available online: https://www.nist.gov/publications/nist-atomic-spectra-database-version-310 (accessed on 7 April 2022).
48. Capitelli, M.; Ferreira, C.M.; Gordiets, B.F.; Osipov, A.I. *Plasma Kinetics in Atmospheric Gases*; Atomic, Optical and Plasma Physics; Springer: Berlin/Heidelberg, Germany, 2000.
49. Gordillo-Vázquez, F.J.; Kunc, J.A. Statistical–mechanical calculations of thermal properties of diatomic gases. *J. Appl. Phys.* **1998**, *84*, 4693–4703. [CrossRef]
50. Berk, A.; Anderson, G.P.; Acharya, P.K.; Bernstein, L.S.; Muratov, L.; Lee, J.; Fox, M.; Adler-Golden, S.M.; Chetwynd, J.H.; Hoke, M.L.; et al. MODTRAN 5: A reformulated atmospheric band model with auxiliary species and practical multiple scattering options: Update. In *Algorithms and Technologies for Multispectral, Hyperspectral, and Ultraspectral Imagery XI*; International Society for Optics and Photonics: Bellingham, WA, USA, 2005; Volume 5806, pp. 662–668.
51. Molina, L.; Molina, M. Absolute absorption cross sections of ozone in the 185-to 350-nm wavelength range. *J. Geophys. Res. Atmos.* **1986**, *91*, 14501–14508. [CrossRef]
52. Minschwaner, K.; Anderson, G.; Hall, L.; Yoshino, K. Polynomial coefficients for calculating O2 Schumann-Runge cross sections at 0.5/cm resolution. *J. Geophys. Res. Atmos.* **1992**, *97*, 10103–10108. [CrossRef]
53. Ripoll, J.F.; Zinn, J.; Jeffery, C.A.; Colestock, P.L. On the dynamics of hot air plasmas related to lightning discharges: 1. Gas dynamics. *J. Geophys. Res. Atmos.* **2014**, *119*, 9196–9217. [CrossRef]
54. Ripoll, J.F.; Zinn, J.; Colestock, P.L.; Jeffery, C.A. On the dynamics of hot air plasmas related to lightning discharges: 2. Electrodynamics. *J. Geophys. Res. Atmos.* **2014**, *119*, 9218–9235. [CrossRef]

55. Pérez-Invernón, F.J.; Luque, A.; Gordillo-Vazquez, F.J. Modeling the chemical impact and the optical emissions produced by lightning-induced electromagnetic fields in the upper atmosphere: The case of halos and elves triggered by different lightning discharges. *J. Geophys. Res. Atmos.* **2018**, *123*, 7615–7641. [CrossRef]
56. Da Silva, C.; Sonnenfeld, R.; Edens, H.; Krehbiel, P.; Quick, M.; Koshak, W. The plasma nature of lightning channels and the resulting nonlinear resistance. *J. Geophys. Res. Atmos.* **2019**, *124*, 9442–9463. [CrossRef]
57. Wang, D.; Takagi, N.; Watanabe, T.; Rakov, V.; Uman, M.; Rambo, K.; Stapleton, M. A comparison of channel-base currents and optical signals for rocket-triggered lightning strokes. *Atmos. Res.* **2005**, *76*, 412–422. [CrossRef]
58. Zhou, M.; Wang, D.; Wang, J.; Takagi, N.; Gamerota, W.; Uman, M.; Jordan, D.; Pilkey, J.; Ngin, T. Correlation between the channel-bottom light intensity and channel-base current of a rocket-triggered lightning flash. *J. Geophys. Res. Atmos.* **2014**, *119*, 13–457. [CrossRef]
59. Zhou, M.; Fan, Y.; Wang, J.; Lu, Y.; Cai, L.; Li, Q.; Fan, Y. Experimental investigation on correlation between fast-front lightning current and the resultant arc channel luminosity. *J. Electrost.* **2020**, *106*, 103455. [CrossRef]